Tracking Coordination Environment and Reaction Intermediates in Homo- & Heterogeneous Epoxidation Catalysts via Ti $L_{2,3}$-edge NEXAFS

Lukas Lätsch,[†] Sergey A. Guda,[§] Vladyslav Romankov,[‖] Christina Wartmann,[#] Jörg-M. Neudörfl,[#] Jan Dreiser,[‖] Albrecht Berkessel,[#] Alexander A. Guda,[§,*] and Christophe Copéret[†,*]

[†] *ETH Zurich, Department of Chemistry and Applied Biosciences, Vladimir-Prelog Weg 2, CH-8093 Zurich, Switzerland*
[§] *The Smart Materials Research Institute, Southern Federal University, Sladkova 178/24, Rostov-on-Don, Russia*
[‖] *Swiss Light Source, Paul Scherrer Institut, CH-5232 Villigen PSI, Switzerland*
[#] *University of Cologne, Department of Chemistry, Organic Chemistry, Greinstraße 4, 50939 Cologne, Germany*

ABSTRACT: Ti-based molecules and materials are ubiquitous, and play a major role in both homogeneous and heterogeneous catalytic processes. Understanding the electronic structures of their active sites (oxidation state, local symmetry and ligand environment) is key to developing molecular-level structure-property relationships. In that context, X-ray absorption spectroscopy (XAS) offers a unique combination of element selectivity and sensitivity to local symmetry. Commonly, for early transition metals such as Ti, K-edge XAS is applied for *in situ* characterization and subsequent structural analysis with high sensitivity towards tetrahedral species. Ti $L_{2,3}$-edge spectroscopy is in principle complementary and offers specific opportunities to interrogate the electronic structure of five-and six-coordinated species. It is, however, much more rarely implemented, because the use of soft X-rays implies ultra-high vacuum conditions. Furthermore, the interpretation of the data can be challenging. Here, we show how Ti $L_{2,3}$-edge spectroscopy can help to obtain unique information about both homogenous and heterogeneous epoxidation catalysts and to develop a molecular-level relationship between spectroscopic signatures and electronic structures. Towards this goal, we first establish a spectral library of molecular Ti reference compounds, comprising various coordination environments with mono- and dimeric Ti species having O, N and Cl-ligands. We next implemented a computational methodology based on multiplet ligand field theory and maximally localized Wannier orbitals benchmarked on our library to understand Ti $L_{2,3}$-edge spectroscopic signatures. We finally used this approach to track and predict spectra of catalytically relevant intermediates, focusing on Ti-based olefin epoxidation catalysts.

INTRODUCTION

Titanium is the second most abundant transition-metal element, and has found numerous applications from white paints to performance functional materials, owing to its versatility, low cost, low toxicity and good biocompatibility.[1] In fact, titanium is used in numerous catalytic homogeneous and heterogeneous processes for the synthesis of fine and bulk chemicals, from epoxidation to hydrofunctionalization and polymerization reactions.[2–4] Notably, Ti-based catalysts are at the center of some of the most prominent industrial processes such as the epoxidation of propylene with Ti-silicates (e.g. TS-1) and the production of polyolefins (e.g. polyethylene and polypropylene) *via* the Ziegler-Natta process ($TiCl_4/MgCl_2$).[5–7]

The nature of the active sites is typically investigated using numerous spectroscopic techniques comprising UV-Visible, IR, Raman, Electron Paramagnetic Resonance, Nuclear Magnetic Resonance and X-ray Absorption Spectroscopy (XAS). These techniques are often used in combination with X-ray diffraction, microscopy, as well as computational modelling.[8,9] Among them, XAS has become a method of choice, especially in heterogeneous catalysis, because it can be used both in quasi *in situ* or operando settings. Furthermore, XAS has profited greatly from recent improvements in terms of infrastructure, instrumentation and computation, including most recently machine-learning approaches.[10] XAS benefits from being element specific and provides detailed information of electronic structures, arising from different transitions, depending on the respective core electrons that are exited through the incident photon beam (K-, L-, M-edge XAS).[11] In addition, XAS provides diverse information at each edge, when focusing on the pre-Edge, the Near-Edge Structure (XANES) and the Extended X-ray Absorption Fine Structure (EXAFS), respectively. XANES is also called Near-Edge X-ray Absorption Fine Structure (NEXAFS), a term typically reserved for soft x-ray absorption spectra, whereas XANES is typically used for the corresponding hard x-ray spectra.

For titanium, both Ti K-edge XANES and Ti $L_{2,3}$-edge NEXAFS are ideally posed to elucidate active-site structures on the molecular level. However, to date, most studies focus on Ti K-edge XANES.[12–16] Characteristic features in Ti K-edge XANES are the pre-edge (quadrupole allowed transitions: 1s→3d and dipole allowed transitions to the 3d states mixed with 4p), near-edge region, including white line (dipole allowed transitions 1s→εp) and post-edge region, usually described in terms of single and multiple scattering processes (Figure 1). These three regions of the spectrum provide independent information about metal charge state and local coordination. Both centroid position and area of the pre-edge are sensitive to the coordination number even without changing the Ti oxidation state.[15,17] Particularly prominent pre-edge features are generally observed for tetrahedral species and are less pronounced for five-or six-coordinated species (no p-d mixing in pure octahedron, *cf.* tetrahedral $[Ti(OTBOS)_4]$ (OTBOS = *tris*(*tert*-butoxy)siloxy) *vs.* octahedral $[TiCl_2(dpm)_2]$ (dpm[18]= dipivaloylmethanate, Figure 1a). In

general, six coordinated species show significantly lower intensity of the pre-edge and thus can remain undetected, especially if mixtures of multiple species are present.

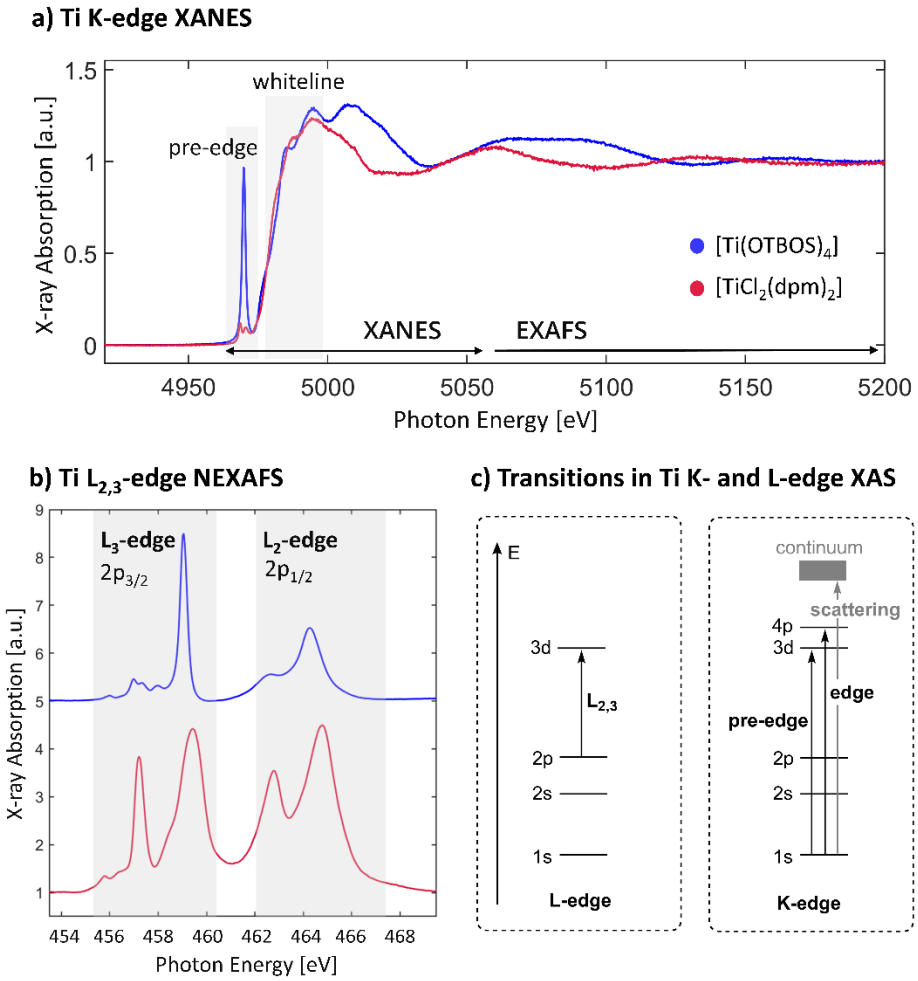

Figure 1: Illustration of spectroscopic signatures of tetrahedral [Ti(OTBOS)$_4$] (blue) and quasi-octahedral [TiCl$_2$(dpm)$_2$] (red). a) Ti K edge XANES, b) Ti L$_{2,3}$ edge NEXAFS and c) schematic representation of transitions relevant to Ti K-and L-edge XAS.

Ti L$_{2,3}$-edge NEXAFS (Figure 1b) should be a complementary tool since it also probes the metal 3d empty final states which contribute to the pre-edge in the K-edge. In Ti L$_{2,3}$-edge NEXAFS, the 2p core level splits into two manifolds due to spin-orbit coupling (L$_2$-edge: 2p$_{1/2}$ at higher energy and L$_3$-edge: 2p$_{3/2}$ at lower energy). The higher intensity of the transitions and better energy resolution compared to K-edge spectroscopy explains the increased sensitivity towards octahedral species. The higher energy resolution originates from the longer life time of the 2p core hole compared to the 1s core hole and better energy resolution of the instrument monochromator at lower energy.[12]

Ti L$_{2,3}$-edge NEXAFS has so far been mostly utilized for solid-state materials with focus on determining the coordination number of Ti atoms, for instance in selenospinel Cu(Cr,Ti)$_2$Se$_4$,[19] Fe-

substituted $CaCu_3Ti_4O_{12}$ ceramics[20] or Ti-silicate glasses.[21] It has also been used to study oxygen vacancies in TiO_2[22] and the solid-liquid interface in TiO_2/H_2O systems.[23] In contrast, Ti $L_{2,3}$-edge NEXAFS has rarely been applied in molecular systems,[24–27] and the interpretation of the spectroscopic signatures has so far remained mostly empirical (by comparison with appropriate solid-state references) or in some cases aided by computation,[28] notably to determine the structure of sodium titanate nanotubes (non-molecular).[29,30] Recent work has extended this spectroscopic technique to studying Ti-based zeolites, where Ti atoms substitute specific positions of the crystalline lattice, and has been proposed to highlight the presence of octahedral sites not readily accessible from K-edge XAS.[31] However, understanding the origin of the observed transitions and their relation to specific electronic structure remains an uncharted territory.

Here, we investigate the Ti $L_{2,3}$-edge NEXAFS of a broad range of molecular Ti complexes in different coordination environments (*e.g.* tetra and hexa-coordinated), with O-, N- and Cl-ligands, as well as monomeric and dimeric structures (*vide infra*), to constitute a representative library of spectroscopic signatures across various coordination environments. We next develop a computational protocol based on maximally localized Wannier functions that accurately reproduces the spectroscopic signatures across the established molecular library. Application of the established computational protocol allowed us to study the conversion of two molecular peroxo complexes and enabled identification of the respective oxo products. Finally, we used our approach to predict the respective spectroscopic signatures of previously proposed intermediates in the titanosilicate-catalyzed epoxidation of propylene.

Results and Discussions

Spectral Library from Well-Defined Molecular Ti-Compounds

We selected nine representative Ti^{IV} complexes (Figure 2) to establish our library. $[Ti(OTBOS)_4]$[32] (**1**) was chosen as a model for tetrahedral sites in titanosilicalite-1 (TS-1), and its related analogue $[Ti(O\mathit{i}Pr)(OTBOS)_3]$[33] (**2**) to study the effect of subtle changes in electronic structure. We also selected $[Ti_2O_2(acac)_4]$[34] (**3**) (acac = acetylacetonate) and $(PPN)_2[OTiP_3O_9(acac)]$[35] (**4**) (PPN = bis(triphenylphosphine)iminium) as octahedral mono- and dinuclear Ti sites, having either bridging or terminal oxo ligands. We also include a family of related molecular complexes, one of them having similar reactivity (Berkessel-Katsuki-Catalyst, BKC, **5**) as TS-1.[36,37] These compounds are based on salen, salan and salalen-type ligands.[37] Depending on whether the nitrogen is part of an imine, secondary or tertiary amine, the ligand can either be tetra-, penta- or hexadentate. The resulting Ti complexes are in turn either dimeric with two bridging μ_2-Os (BKC, **5**), dimeric with one bridging μ_2-O: [Ti-pentadentate-salan] (**6**) or monomeric: [Ti-hexadentate-salan] (**7**). Finally, we evaluated the effect of terminal and bridging chlorido ligands (μ_2-Cl) through comparison with $[TiCl_2(dpm)_2]$[39] (**8**) and $[Ti_2Cl_8(EB)_2]$ (**9**) (EB = ethylbenzoate).

Such compounds are also notable as they have been proposed as potential model of the Ziegler-Natta catalysts and they can help to study subtle changes of environment with the introduction of Cl anionic ligands.[40] With this library in hand, we next measured their respective spectroscopic signatures (Figure 2). Since Ti $L_{2,3}$-edge NEXAFS are based on soft X-rays (454 – 470 eV), all measurements were conducted under ultra-high vacuum (UHV, 10^{-9} mbar). A critical prerequisite is thus the sample stability under these conditions, which is the case for all entries in the molecular library (see ESI Ch. S1 for experimental details).

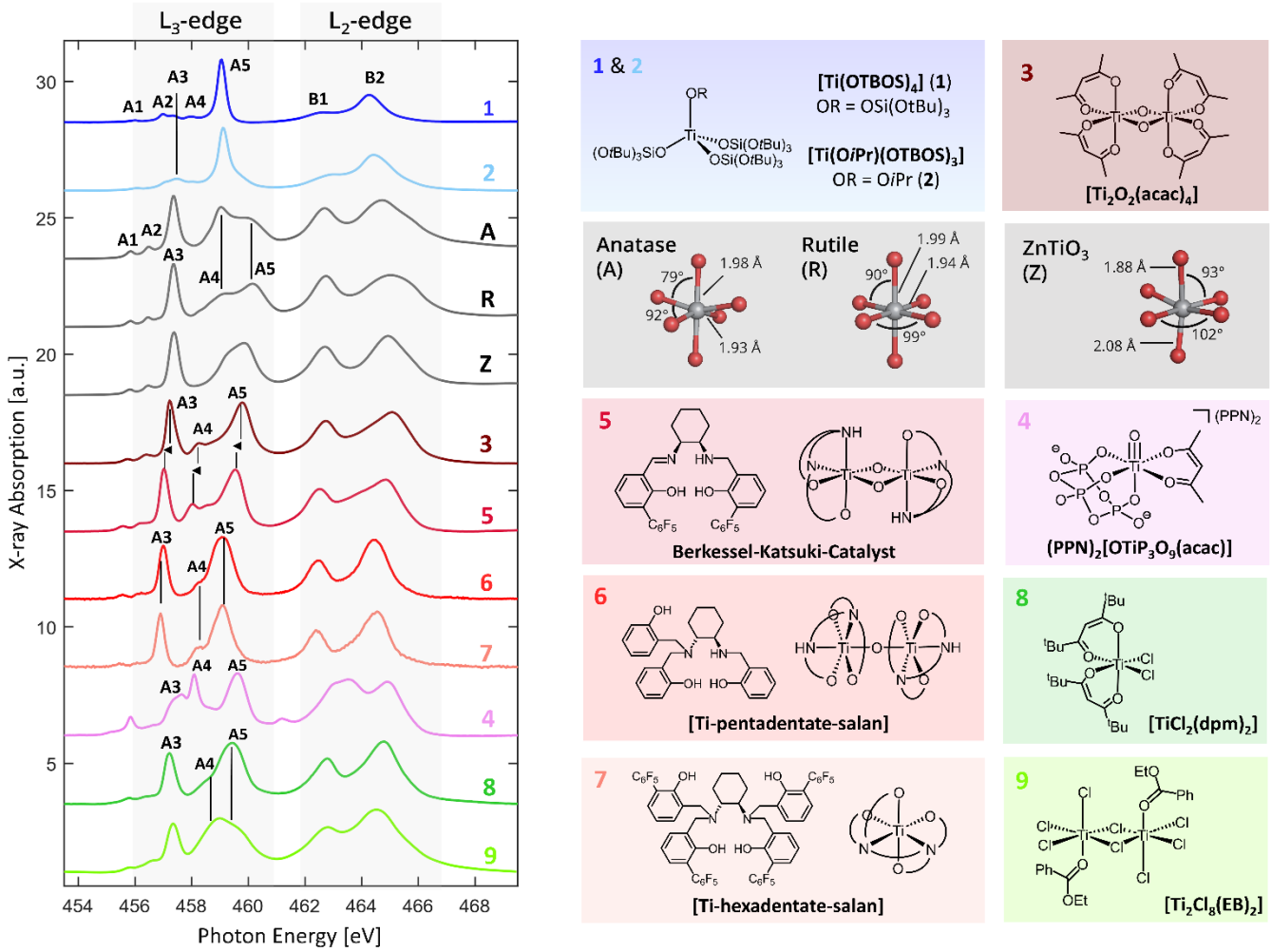

Figure 2: Molecular library chosen to elucidate structure-function relationship: tetrahedral vs. octahedral coordination geometry, influence of oxygen, nitrogen and chlorido-ligands, bridging vs. terminal ligands (for crystal structure codes see ESI Ch. 4.2.) and respective Ti $L_{2,3}$-edge NEXAFS of the molecular library members.

Tetrahedral compound [Ti(OTBOS)$_4$] (**1**) displays a spectroscopic signature with seven peaks associated with the L_3- and L_2-edges that are coined respectively **Ai** and **Bi** transitions in Figure 2. Two intense peaks appear at 459 eV (**A5**) and 464 eV (**B2**), along with a number of lower intensity peaks 456 eV (**A1**), 457.0 eV (**A2**), 457.3 eV (**A3**) and 458.0 eV (**A4**) as well as 462.5 eV (**B1**). Notably, the signature is

significantly affected upon substitution of only one of the siloxy ligands in [Ti(O*i*Pr)(OTBOS)$_3$] (**2**). While no changes are observed for the **A2** and **A4** features, the **A3** and **B1** features increase in intensity and a shoulder from the **A5** feature emerges at 459.8 eV. Moving to the octahedral dimeric compound [Ti_2O_2(acac)$_4$] (**3**) leads to a dramatic change of signature with prominent **A3** and **B1** features in addition to **A5** and **B2**, contrasting what is observed for the tetrahedral system. Note that other frequently used octahedral Ti^{4+} references such as TiO_2 polymorphs contain differently distorted Ti sites: they display similar **A1**-**A3** features, however, the **A4** and **A5** peaks vary in intensity due to the decreased symmetry. Notably, anatase and rutile can easily be distinguished through the ratio of their respective **A4**/**A5** features. In fact, for comparison, the **A4**/**A5** ratio is much smaller in the more regular octahedron of [Ti_2O_2(acac)$_4$] (**3**). Notably, this feature can also be used to probe the local structure and specific phase of $ZnTiO_3$, which can adopt either a rhombohedral "ilmenite" structure (Ti-O_6 octahedra are arranged similarly as in rutile) or a cubic perovskite structure (three-dimensional network closer to anatase TiO_2). In our work, the measured $ZnTiO_3$ reference has an ilmenite structure, as evident from its spectroscopic signature (in particular **A4**/**A5** features).[41] In addition, and in contrast to all three solid-state references, [Ti_2O_2(acac)$_4$] (**3**) shows a moderate, but strongly shifted **A4** feature at 458.2 eV (shifted towards lower energy, see ESI Fig. S1 for comparison with solid-state references). There are a few molecular titanyl complexes where the oxo ligand is not bridging but terminal (Ti-O triple bond), one such example being (PPN)$_2$[$OTiP_3O_9$(acac)] (**4**).[35] Compound **4** displays an even more pronounced **A4** feature than the bis-μ_2-oxo complex **3** at similar (low) energy. The observed differences are accompanied by an increased **A1** and smaller **A3** feature, respectively.

The Berkessel-Katsuki-Catalyst (BKC, **5**) shows a spectroscopic signature remarkably similar to [Ti_2O_2(acac)$_4$] (**3**), with all peaks shifted to lower energy (ΔE = 0.2 eV). This is likely a reflection of their structural similarity, with both complexes possessing two bridging μ_2-oxo ligands. The shift towards lower energy for the BKC (**5**) can be rationalized with nitrogen being a less electronegative ligand than oxygen. To further probe the influence of specific structural motives on the spectroscopic signature, we synthesized the corresponding [Ti-pentadentate-salan] (**6**), a dinuclear salan complex with only one μ_2-oxo ligand and [Ti-hexadentate-salan], the corresponding monomer (**7**, for synthetic details see ESI Ch. S3). In this series, the **A3** and **A5** peaks shift gradually to lower energy with exception of the **A4** peak, that is most distinguishable for the bis-μ_2-oxo complexes **3** and **5**. This shift to lower energy can be rationalized by the presence of less electronegative ligands (non-fluorinated for [Ti-pentadentate-salan] (**6**)) or the absence of oxo ligands ([Ti-hexadentate-salan] (**7**) yielding a less electropositive metal center). Finally, to evaluate the effect of chlorido ligands we also studied [$TiCl_2$(dpm)$_2$] (**8**) with two terminal *cis*-chlorido ligands and [Ti_2Cl_8(EB)$_2$] (**9**) with two bridging μ_2-chlorido ligands. Their spectroscopic

signature again mainly differs in the ratio of the **A4**/**A5**-peaks, with $[Ti_2Cl_8(EB)_2]$ displaying a more pronounced **A4** feature and $[TiCl_2(dpm)_2]$ having a more pronounced **A5** feature, respectively.

Qualitative View on the Spectral Features in Ti $L_{2,3}$-edge NEXAFS

From a theoretical point of view, the fine structure in Ti $L_{2,3}$ spectra can be explained through the interplay of spin-orbit coupling, multiplet interactions, crystal-field splitting, band structure and charge transfer effects.[42–46] These effects complicate the interpretation of each transition in terms of one-electron molecular orbitals. In the following discussion, we address the relationship between local atomic structure and spectral features on the basis of empirical crystal-field and ab initio multiplet ligand-field theory using Wannier orbitals. Basic trends are shown in Figure 3 for the simulation of the Ti^{4+} $3d^0 - 2p^53d^1$ transition in octahedral or tetrahedral coordination (positive and negative 10 Dq values correspondingly, see ESI Ch. 4.1 for computational details). The ground state of the Ti^{4+} d^0 system is described by one single $^1S_0$ term. The excited $2p^53d^1$ state comprises couplings between 6 microstates on the $2p^5$ shell and 10 microstates on the $3d^1$ shell, resulting in a total of 60 final microstates. In spherical symmetry, these microstates are grouped into 12 term symbols when spin-orbit interaction is included. The dipole selection rule requires $\Delta J = +1, 0, -1$ excluding $J_i = J_f = 0$ - thus only $^1P_1$, $^3P_1$ and $^3D_1$ terms with a total angular momentum J=1 can be probed upon X-ray absorption. These terms are mixed into three energy levels due to spin-orbit coupling and explain three peaks in the Ti^{4+} $L_{2,3}$ spectrum with 10Dq=0 (middle green curve in Figure 3). The intensity of each transition is determined by the contribution of the $^1P_1$ state in the corresponding energy level. In a cubic crystal field, the microstates with defined J-values are further split into A_1, A_2, T_1, T_2 and E representations of the O_h symmetry group. The selection rules allow then only transitions into microstates with T_1 character since J = 1 correlates to T_1 upon descent in symmetry from O_3 into O_h. However the T_1 irreducible representation can also be reached from J=3 and J=4.[42] Degeneracies of microstates with allowed J explain seven peaks in a spectrum with finite 10Dq (peaks **A1**-**A5** and **B1**-**B2**). At large crystal field four lines dominate in the spectrum. These lines may be assigned to one-electron transitions as demonstrated by the top and bottom gray spectra (calculated with reduced Slater-Condon integrals, *i.e.* omitting 2p-3d interaction). In one-electron approximation, **A3** and **B1** peaks thus correspond to t_{2g} level while **A5** and **B2** to e_g level (with the ratio of intensities **A3**:**A5** = **B1**:**B2** = 3:2 in a octahedral field).

The local geometry and covalency of ligands change the energy splitting between peaks and their relative intensity. The negligible intensity of **A3** and **B1** with respect to **A5** and **B2** at low 10Dq has a multiplet origin. Without interaction with the 2p core hole, the crystal field splits each of the L_2 and L_3 peaks into two intensive lines as shown in the upper scheme in Figure 3. The new peaks appearing in the

spectrum of the $2p^5 3d^1$ multiplet in the crystal field are explained by mixing and do not arise from splitting. Coulomb interactions between the 2p hole and 3d electron create 12 microstates in the spherical symmetry, only three of which can be probed in Ti $L_{2,3}$ spectroscopy. The crystal field reduces the degeneracy of states and creates 25 microstates, of which only seven of which are dipole allowed.

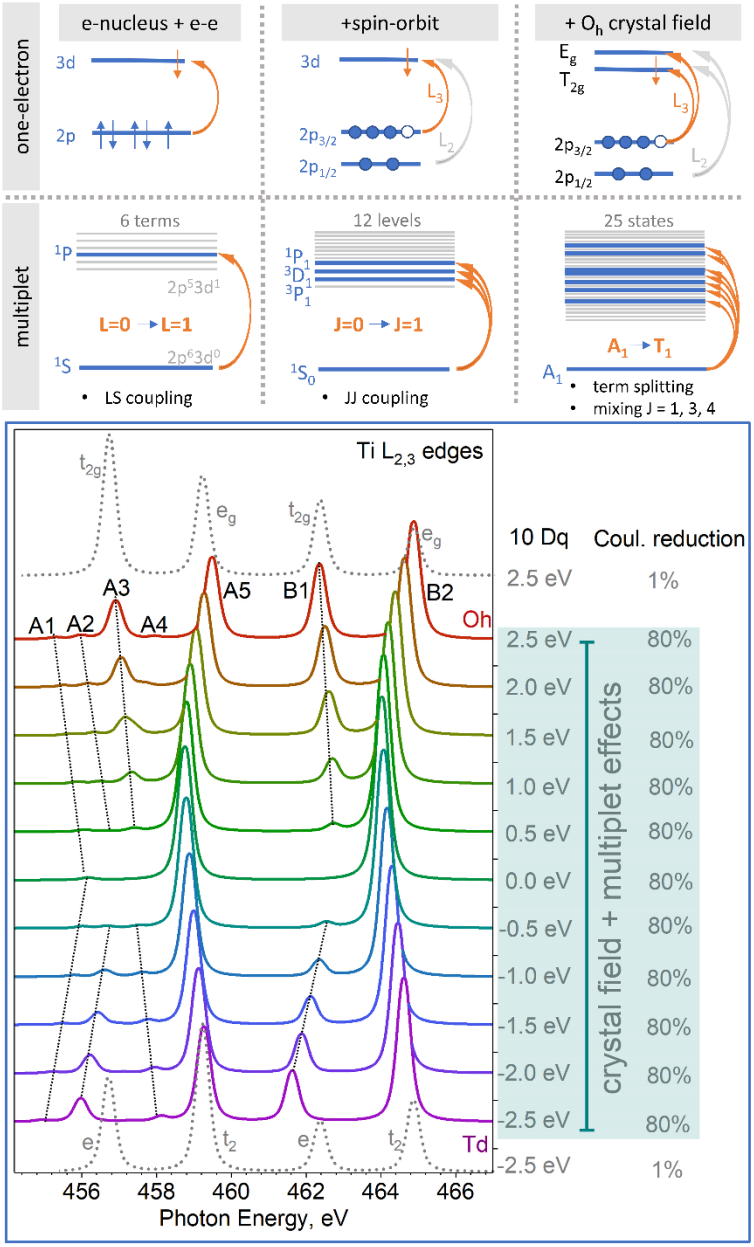

Figure 3. Upper panel: scheme for one-electron and multiplet transitions in Ti^{4+}. Blue lines indicate allowed transitions, and gray levels multiplet terms. Bottom panel: Crystal field multiplet calculations for the $3d^0 - 2p^5 3d^1$ transition in Ti^{4+} using different 10Dq values. Positive crystal field values correspond to the octahedral symmetry and negative ones to the tetrahedral or cubic symmetry (note that for equal charges in the corners of the polyhedron the splitting value for tetrahedral coordination equals -4/9 of octahedral one). The most intense peaks for large crystal field splitting are assigned to the one-electron irreducible representations of O_h and T_d groups.[45]

The seven transitions include four final microstates that were dipole-forbidden but become visible due to mixing with the $^1P_1$ term. Increasing 10Dq changes the energy of multiplets and in particular increases the contribution of $^1P_1$ into **A3** and **B1** terms (see also Figures 3-6 in ref [42]). Peak **A4** has a multiplet origin and appears already in an ideal O_h symmetry as shown in Figure 3. In the series of reference spectra for quasi-octahedral compounds (Figure 2) its intensity depends on the ligand environment. The intensity may also increase dramatically upon overlap with satellites of the **A5** peak that appear for distorted environments (see ESI Fig. S20 for calculation of D_{4h} vs. O_h crystal field). Another effect observed in experiments and related to many-body interactions is the larger broadening of features in the L_2-edge if compared to L_3 (see Figure 2). The full theoretical description should include charge transfer effects in multiplet calculations[24,45] or excitonic effects in band structure calculations[43] that prevent the specific assignment of spectral features in terms of one-electron molecular orbital transitions. Apart from the peak position and intensity, we note that the integrated intensity of the L-edge is another useful descriptor of the metal-ligand bond covalency and differential orbital covalency. Wasigner *et al.* have utilized X-ray absorption spectra to quantify these parameters[47] while Lundberg *et al.* and Kroll *et al.* extended the methodology to 1s2p resonant inelastic X-ray scattering.[48,49] In our work we address the metal 3d – ligand 2p hybridization theoretically upon constructing local Hamiltonian model on the basis of maximally localized Wannier functions (*vide infra*).

In our library, we observed the appearance of a high energy shoulder of peak A5 when substituting one siloxide ligand by one alkoxide ligand (*cf.* $[Ti(OTBOS)_4]$ (**1**) *vs.* $[Ti(OiPr)(OTBOS)_3]$ (**2**), for overlay see ESI Fig. S1). These findings are in line with the reduced symmetry and the alkoxide being a less electronegative ligand forming a slightly more covalent bond and hence giving rise to a larger e_g- t_{2g}-splitting (ca. 0.4 eV). The larger crystal field splitting also accounts for the intensity increase of the **A3** feature (*vide supra*). Overall, the crystal field splitting for the two tetrahedral complexes is still rather small when compared to the octahedral complexes studied herein, as can be deduced from the appearance of both intense **A3** and **A5** features for complexes **3-9** (see Figure 2). For $[Ti_2O_2(acac)_4]$ (**3**) and in contrast to solid-state reference such as anatase, rutile or $ZnTiO_3$, we noticed a moderate **A4** feature at relatively low energy (458.2 eV). In a simplified crystal-field picture, this feature results from the bridging oxo-ligands as a consequence of the strong hybridization with the former anti-bonding e_g-orbitals. For $(PPN)_2[OTiP_3O_9(acac)]$ (**4**), where the Ti-O fragment is best described as a triple bond (Ti≡O), orbitals from both the e_g and t_{2g} set are involved, resulting in the d_{x2-y2}, d_{xy} and d_{yz} being close in energy[50] and giving rise to an even more pronounced **A4** feature than for $[Ti_2O_2(acac)_4]$ (**3**) (see ESI Ch. 4.5. for illustration). In accordance with this assignment, previous studies of the electronic structure in titanyl phthalocyanine show an enhanced intensity for the peak labeled as **A4** in our notation.[27] The

aforementioned study investigated the influence of replacing the titanyl ligand by a catechol-based bidentate ligand, which retains most of the electronic structure, apart from the inversion of d_{z2} and d_{x2-y2} orbitals, hence overall yielding a similar signature.

DFT based Ligand Field Computational Protocol

The spectroscopic signatures show great sensitivity towards small structural changes and can in part be directly linked with specific functional groups. However, due to the complexity of multiplet effects in the spectra, further theoretical calculations are needed to further support these assignments. Moreover, the development of a computational protocol that can reproduce the observed features will help greatly to assign active site structures in heterogeneous catalysts. Existing approaches may be divided into three categories.[46] The first one includes semi-empirical multiplet codes,[51–55] that require specifying both crystal field parameters (structure specific) and parameters related to the electronic system. Such an approach can hardly be applied to the arbitrary coordination of metal centers since it requires parametrization of the energy splitting between metal d- and ligand orbitals. This methodology is improved in the ligand-field DFT approximation[56] where parameters of the local Hamiltonian are evaluated from a molecular orbital approach[57] or band structure calculations.[53] Finally the third category approaches is based on ab-initio high level of theory, including the Bethe-Salpeter equation,[58] dynamic mean-field theory LDA+DMFT,[59] multi-channel multiple scattering[44] and post Hartree-Fock methods.[24,60] However, it is highly demanding in computational resources and thus may hardly be applied to metal complexes with bulky ligands or multinuclear complexes.

In our work we rely on the ligand-field + DFT methodology. Scheme 1 illustrates the typical workflow for the $[TiCl_2(dpm)_2]$ (**8**) molecule. The molecule is placed inside a supercell with sufficient surrounding vacuum, and its electronic structure is calculated self-consistently within DFT/GGA-PBE approximation[61] using only one k-point in reciprocal space. To balance accuracy and computational costs, we simplified studied models by removing all atoms further than the second coordination sphere through H-termination. In the case of multidentate ligands, we have kept the carbon backbone for more accurate modelling of the electronic structure. During the structure optimization step, only the position of the H-atoms introduced for termination were allowed to be optimized (see ESI Ch. 4.3. for computational details). For $(PPN)_2[OTiP_3O_9(acac)]$ (**4**), we replaced the cations by protons in the vicinity of the metaphosphate-ligand.

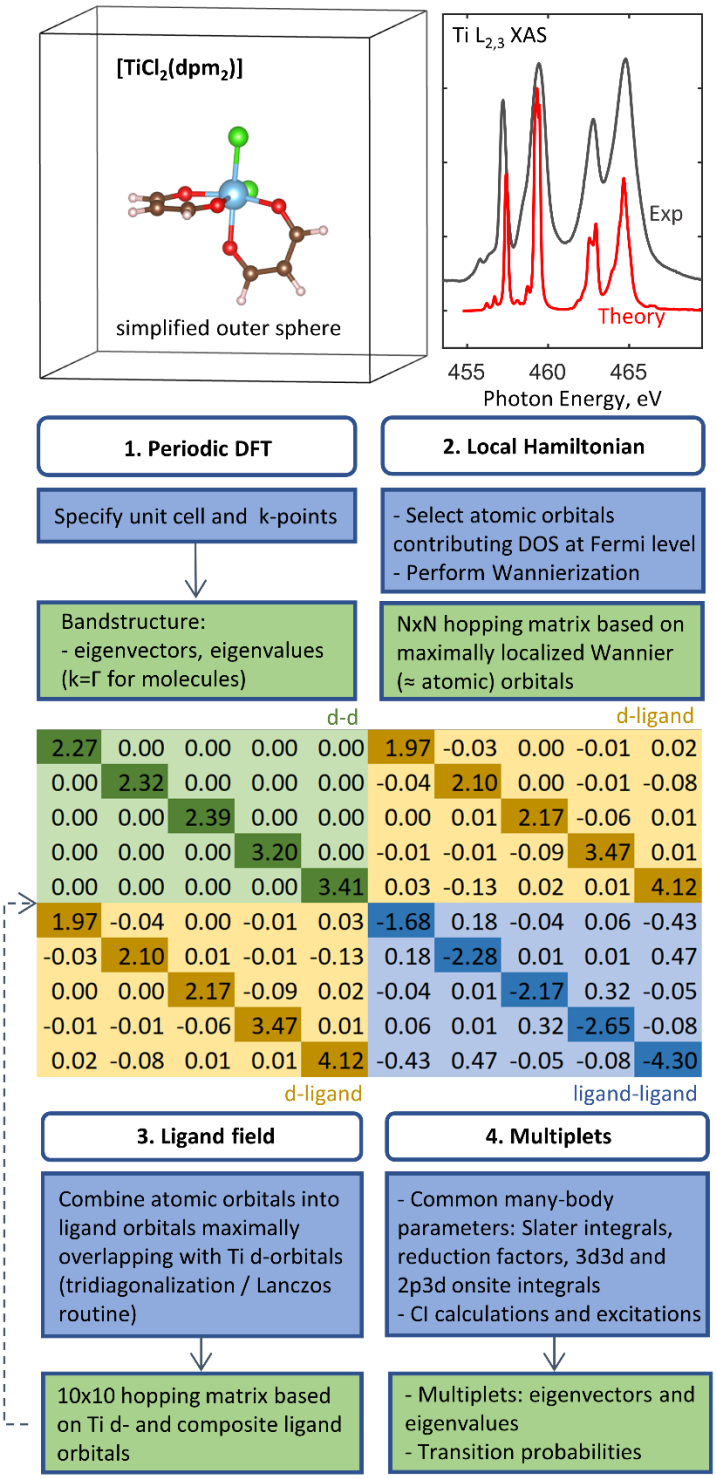

Scheme 1: Multiplet ligand-field computational methodology applied for Ti molecular complexes including bandstructure calculation, Wannerization and Lanczos transformation as exemplified for $[TiCl_2(dpm)_2]$ (**8**). For full benchmarking on the established molecular library see ESI Ch. 4.4. Middle part: Fragment of the local Hamiltonian matrix constructed on the basis of maximally localized Wannier functions after tridiagonalization transformation. The upper left 10x10 corner specifies the hopping matrix elements between Ti d-states and composite ligand orbitals. For further details refer to Section S4.3 in ESI and ref[53].

In the second step ("Local Hamiltonian" in Scheme 1), the energy range of the nearby valence band and contributing atomic orbitals are selected from careful analysis of the density of states. The strategy is to select only those ligand states that hybridize with metal d-states. For $[TiCl_2(dpm)_2]$ (**8**) these were five Ti d-orbitals, six chlorine p-orbitals, twelve oxygen p-orbitals and 18 carbon p-orbitals. Note that bulkier molecules additionally require the use of s- and p-orbitals of more distant atoms that fall within the energy region of Ti d-states. These atomic orbitals are specified in the Wien2wannier program and used as initial approximation to construct maximally localized Wannier functions (MLWF)[62] in the Wannier90 program. Properly derived MLWF describe the whole bandstructure inside the selected energy region (see ESI Ch. 4.3.3. for the complete list of projector atomic orbitals and energy regions for each molecule). The local Hamiltonian matrix is constructed on the basis of hopping matrix elements between MLWF.

In the third step ("Ligand Field" in Scheme 1) the large local Hamiltonian matrix is reduced into 10x10 size by constructing composite ligand orbitals *via* a tridiagonalization step.[53] The matrix elements along the side diagonal (orange d-ligand blocks in Scheme 1) represent the covalent interaction between metal d-orbitals and ligand orbitals. All the hopping matrix elements between metal d-states and ligand p-states (10x10 colored block in Scheme 1) are applied for the full-multiplet configuration-interaction calculations implemented in XTLS code.[51] The DFT-based ligand field multiplet calculations account for the atomic 3d–3d and 2p–3d Coulomb interactions, 2p and 3d spin-orbit couplings, the local crystal field, and the O 2p–Ti 3d hybridization. This hybridization is included via charge-transfer effects by adding the $3d^{n+1}\underline{L}$ and $3d^{n+2}\underline{L}^2$ to the starting $3d^n$ configuration, where L denotes a hole in ligand orbital (see Section S4.3 in ESI for further details and example of the XTLS input file). The spectrum is calculated iteratively using the Lanczos algorithm and the spectral function. The computed amplitudes are convoluted with a Lorentian and Gaussian broadenings (0.04 eV each, see Figure S21 in the ESI for the whole set of benchmark calculations and with increasing profile width for Figure 4 from 0.2 to 0.6 eV to match the experimental curves). Spectroscopic signatures show overall good agreement with the experimental.

Molecular (Per)oxo Ti $L_{2,3}$-edge NEXAFS Signature

Only few spectroscopic techniques can easily distinguish between mononuclear and μ_2-bridging peroxo groups. However, identification of such intermediates is of prime importance for the rational development of new and improved oxidation catalysts.[63] Given the results obtained and the general sensitivity of Ti $L_{2,3}$-edge NEXAFS towards small changes in octahedral coordination environments in conjunction with the establishment of a suitable computational protocol, we investigated the corresponding molecular peroxo compounds. These include the BKC-peroxo (**10**, Figure 4), a dinuclear η^2,μ^2-peroxo complex and $[TiCl_2(\eta^2\text{-}O_2)(bdmpp)]$ (**11**, bdmpp = 6-bis(3,5-dimethyl-N-pyrazolyl)-pyridine)[64], a mononuclear peroxo

complex. Whereas no catalytic activity has been reported for $TiCl_2(\eta^2\text{-}O_2)(bdmpp)]$ (**11**), the BKC-η^2,μ^2-peroxo-complex **10** corresponds to the resting state of the Berkessel-Katsuki catalyst **5**.[37] Crystal structures of both peroxo complexes have been reported.[36,64] One major challenge in the characterization of peroxo-species is their relatively low stability. Hence, measurement conditions must be designed carefully to prevent decomposition of the peroxo-complex (only few scans, reduced spot size). Interestingly, the decomposition product of the BKC-peroxo **10** is the parent BKC complex **5** (Figure 4). The characterization of the peroxo intermediate **10** is further validated through the computed spectroscopic signature, that predicts the same trend. Compared to the parent BKC **5**, the BKC-peroxo **10** shows a reduced **A3** feature and increased intensity of the **A4** feature. This can be understood in terms of the ligand effect on the crystal field splitting. The peroxo-moiety induces a smaller crystal field splitting than the oxo-ligand (as can also be deduced from the relative bond-distances, with the Ti-O bond being shorter for the bis-oxo-complex) and hence gives rise to a smaller **A3** feature. The increase in intensity of the **A4** feature is due to the reduction of symmetry that further lifts the degeneracy of the former e_g-orbitals (Fig. S24).

For the mononuclear $[TiCl_2(\eta^2\text{-}O_2)(bdmpp)]$ (**11**), the measured spectra show an **A3** feature with even further reduced intensity, only a small **A4** feature and a dominant **A5** feature. In the case of the mononuclear peroxo **11**, the crystal field splitting induced by the ligands is thus so weak that its **A3** peak is similar to the tetrahedral references studied herein. Hence, it can easily be distinguished from the μ_2-bridging peroxo (as in the BKC peroxo **10**, Figure 4) as a consequence of the different degree of crystal field splitting being induced by the type of peroxo-ligand (primarily due to weaker bonding of the peroxo-ligand with the Ti, arising from π-orbitals only). For $[TiCl_2(\eta^2\text{-}O_2)(bdmpp)]$ (**11**), the resulting decomposition product is likely the oxo-derivative **12**, displaying a similar spectroscopic signature as $(PPN)_2[OTiP_3O_9(acac)]$ (**4**). The assignment is consistent with the computed spectroscopic signature of $[TiCl_2(O)(bdmpp)]$ (**12**). For $[TiCl_2(\eta^2\text{-}O_2)(bdmpp)]$ (**11**), the small discrepancy between calculated and measured spectroscopic signature can be explained through partial beam damage already in the first scans. Overall, it highlights the importance of a combined experimental and computational approach for the characterization of reactive intermediates.

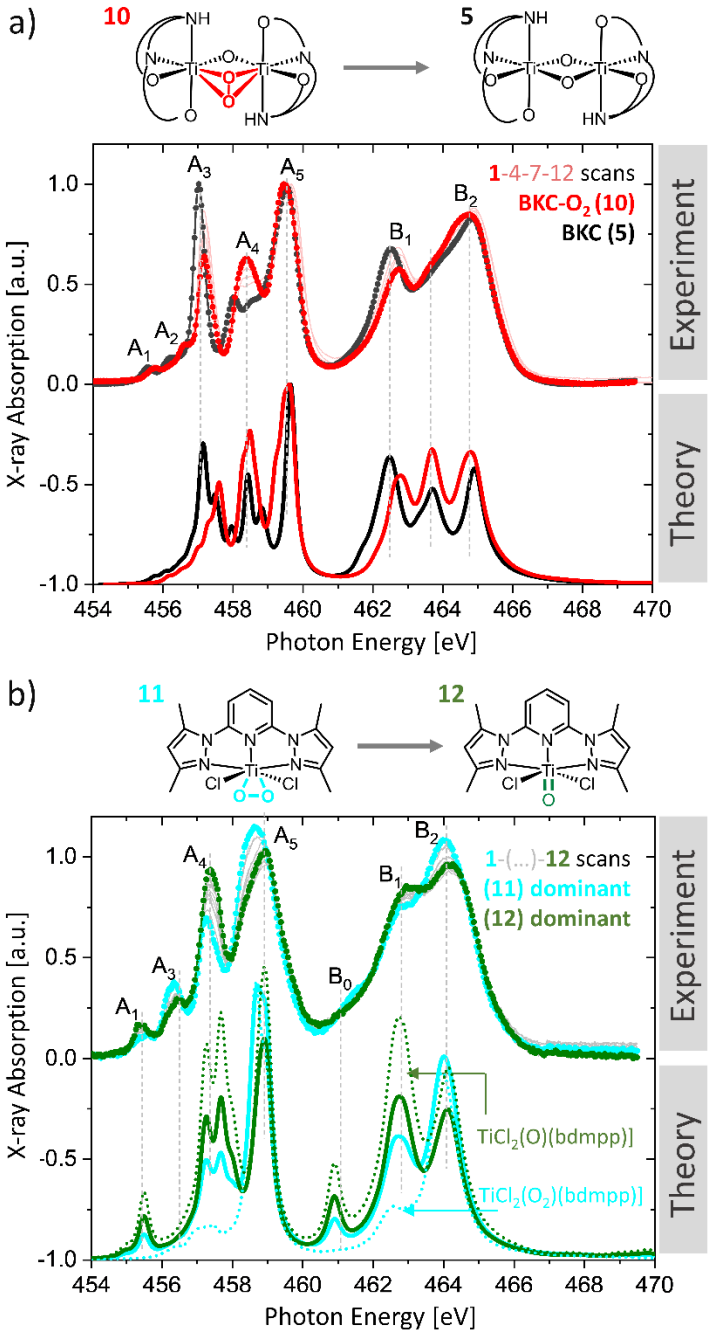

Figure 4: BKC-peroxo **10** (top) and [$TiCl_2(O_2)$(bdmpp)] (**11**) (bottom) decomposition through irradiation. The reaction products can be identified as the corresponding oxo derivatives *via* comparison with molecular models and through computation, respectively.

Prediction of the Spectroscopic Signature of Ti-sites in TS-1 Epoxidation Catalysts and Reaction Intermediates

Next, after having demonstrated the viability of the methodology for molecular complexes, we revisited the titanosilicate catalyzed epoxidation of propylene. Although Ti $L_{2,3}$-edge NEXAFS has been used to analyze octahedral defects in TS-1,[24] no tetrahedral reference has been measured for comparison. From

our library, the crystal structure of [Ti(OTBOS)$_4$] (**1**) shows near perfect tetrahedral symmetry in the first and second coordination sphere, which is rare for heterogeneous materials as recently exemplified by $^{47/49}$Ti solid-state NMR spectroscopy.[32] In comparison, for a prototypical TS-1 sample – where all previous characterizations have found no extra-framework TiO_2 – we have measured a significantly broader **A5** feature than for [Ti(OTBOS)$_4$] (**1**) (0.3eV at FHWM for **1** and > 0.6 eV for extra-framework Ti free "perfect" TS-1, see Figure 5a).[19,31] While this is in part due to small structural variation of the various T-sites (as exemplified by a computational screen of bond-distance and angle variation, see Figure 5a), it mostly arises from very small fractions of octahedral defects / extra-framework Ti that are not detected in Ti K-edge XANES or $^{47/49}$Ti solid-state Ti NMR spectroscopy. In line with this assignment, the TS-1 spectrum also demonstrates a higher integrated intensity compared to the tetrahedral reference [Ti(OTBOS)$_4$], however, due to the limited accessible normalization range we do not compare these values quantitatively. Similarly, and in contrast to previous studies,[31] our modelling conclusively shows that one cannot rule out the occurrence of dinuclear Ti sites within the framework based on the Ti $L_{2,3}$-edge NEXAFS signature (Figure 5a and ESI Ch. 4.6 for details) because mono- and dinuclear sites have similar transitions (energy/transition) that are mostly associated with their very local coordination geometry.

Moving further, we aim to explore Ti $L_{2,3}$-edge NEXAFS as a tool to investigate the fate of Ti in TS-1 once it has been contacted with hydrogen peroxide. Previous studies by some of us using ^{17}O solid-state NMR spectroscopy to analyze the activated TS-1 sample showed the presence of one single species assigned to a μ_2-peroxo.[63] Direct evidence for having two Ti sites involved would need a complementary spectroscopic technique directly probing the metal sites. If the various proposed reaction intermediates could be assigned based on Ti $L_{2,3}$-edge NEXAFS, it would motivate to develop an adequate pseudo *in situ* setup that is currently not available. We have thus calculated the NEXAFS signatures of various reaction intermediates, namely Ti-oxo, mono- or dinuclear (μ_2-bridging) peroxos, hydroxo or hydroperoxos species, in order to evaluate the possibility to use this approach in further studies. Calculated Ti $L_{2,3}$-edge NEXAFS spectroscopic signatures (Figure 5b) show distinct features for all sites proposed. In general, quasi-octahedral species show a shift of the **A5**/**B2** features towards higher energy in line with the higher 10 Dq value, most strongly pronounced for the μ_2-bridging peroxo. The lowest crystal-field splitting (with only a small **A3** feature remaining) is calculated for the hydroperoxo. Overall, calculated spectroscopic signatures for the mono- and di-nuclear η^2,μ^2-peroxo species predicted for TS-1 upon H_2O_2 activation are very similar to the molecular models studied in this work (*vide supra*), further highlighting the ability of Ti $L_{2,3}$-edge NEXAFS to discriminate the respective species.

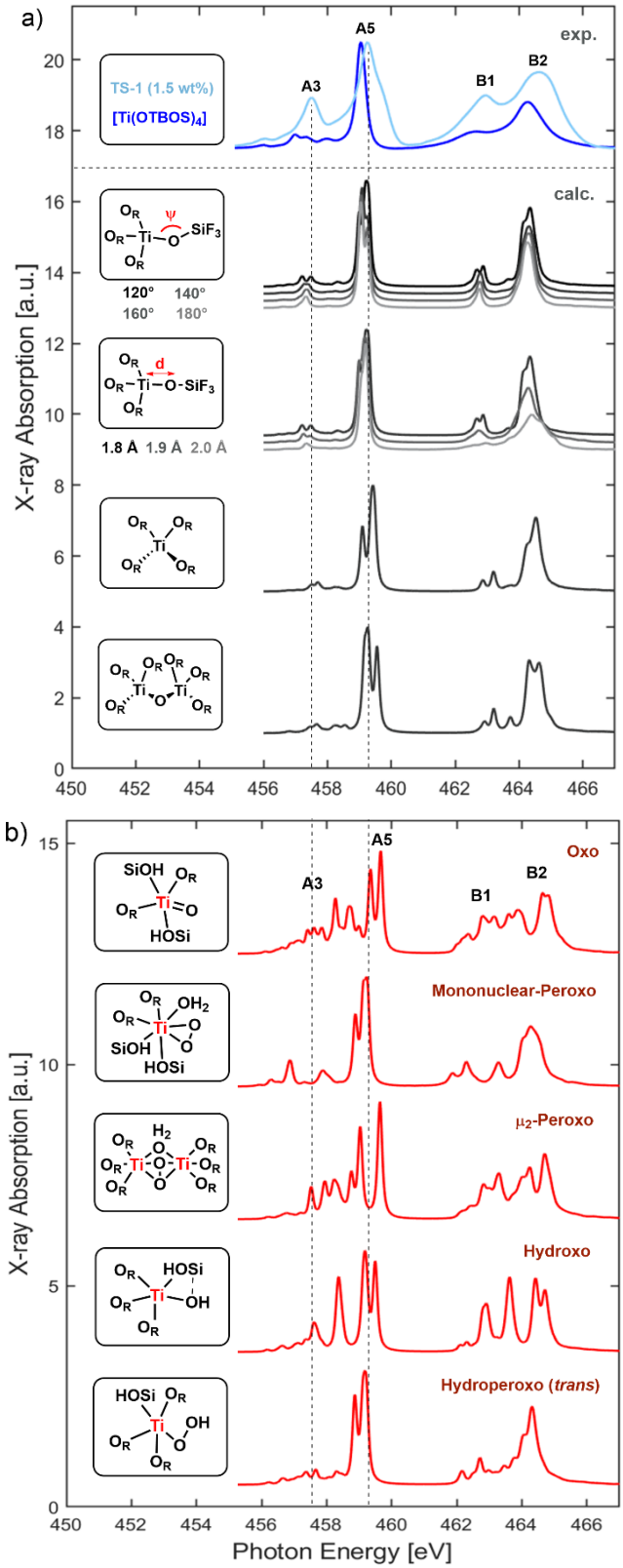

Figure 5: a) TS-1 (before exposure to H_2O_2) vs. tetrahedral molecular model [Ti(OTBOS)$_4$] and computed Ti $L_{2,3}$ edge NEXAFS spectroscopic signatures of distorted tetrahedral sites as function of Ti-O-Si bond angles and distances as well as comparison between mono-and dinculear models. b) DFT calculated Ti $L_{2,3}$ edge NEXAFS spectroscopic signatures of intermediates in the titanosilicate-catalyzed epoxidation of propylene (red, after exposure to H_2O_2). O_R denotes $OSiF_3$ moieties.

Conclusions

Overall, Ti $L_{2,3}$-edge NEXAFS offers molecular-level detailed information regarding the structure of active sites in both molecular and heterogeneous catalysts, albeit requiring very pristine high vacuum conditions. In particular, the development of a spectral library based on a range of well-defined Ti^{IV} complexes differing in their coordination environment and nuclearity has been key to highlight the sensitivity of the Ti $L_{2,3}$-edge NEXAFS spectroscopic signatures towards small structural changes. The recorded spectral library enabled the identification of crystal field splitting as a key descriptor. While it readily allows to distinguish different coordination environments and ligand types (based on their different ligand electronegativity), this approach cannot be used to distinguish more subtle differences, such as the presence of mono- and di-nuclear Ti sites in TS-1.

The computational protocol implemented in this work, based on maximally localized Wannier functions for molecular species, is able to accurately reproduce the spectroscopic signatures across the whole established molecular library and thus allows to accurately calculate and predict spectral signatures. In the specific context of olefin epoxidation, one can identify and track the conversion of peroxo into oxo reaction intermediates. The spectroscopic characterization of both the BKC peroxo complex and of the mononuclear Ti peroxo showed that distinguishing between terminal η^2-peroxo from dinuclear μ^2,η^2-peroxo is possible with Ti $L_{2,3}$-edge NEXFAS because of the lower crystal field splitting in terminal vs. bridging peroxo moieties. We also show that in principle one should be able to track the reaction intermediates in TS-1 epoxidation catalysts, *e.g.* Ti-oxo, mono- and dinuclear peroxo complexes, from the analysis of Ti $L_{2,3}$-edge NEXAFS – further motivating the development of an adequate low temperature cell, a path that we are currently exploring.

ASSOCIATED CONTENT

CCDC 2306102 and 2306103 contain the supplementary crystallographic data for this paper. These data can be obtained free of charge via www.ccdc.cam.ac.uk/data_request/cif, or by emailing data_request@ccdc.cam.ac.uk, or by contacting The Cambridge Crystallographic Data Centre, 12 Union Road, Cambridge CB2 1EZ, UK; fax: +44 1223 336033.

AUTHOR INFORMATION

Corresponding Authors

* Christophe Copéret: ccoperet@ethz.ch.
* Alexander Guda: guda@sfedu.ru

CONFLICT OF INTEREST

The authors declare that they have no conflict of interest.

ACKNOWLEDGMENT

L.L. thanks the Scholarship Fund of the Swiss Chemical Industry (SSCI) for funding. The work conducted at ETH Zürich was partially funded by BASF, and we thank Dr. A.-N. Parvulescu, Dr. T. De Baerdemaeker and Dr. J. H. Teles for helpful discussions. The Swiss Norwegian beamlines (SNBL, ESRF) are acknowledged for provision of beamtime through proposal 31-01-143 (Ti K edge XANES). We thank Dr. W. van Beek and Dr. D. Stoian for their support during XAS experiments and D. Pashkov from the Smart Materials Research Institute for his valuable help in programming automatizing scripts for LAPW and Wannierization calculations. Y. Stiefel and Dr. A. Yakimov are acknowledged for the synthesis of complex **4** and **9**, respectively. A.G. acknowledges the financial support from the Ministry of Science and Higher Education of the Russian Federation (State assignment in the field of scientific activity, № FENW-2023-0019). C.W. thanks the Fonds der Chemischen Industrie (FCI) for a Kekulé doctoral fellowship. J.D. and V.R. thank the Swiss National Science Foundation for financial support (grant no. 200020_182599). This work was carried out as part of NCCR Catalysis (grant number 180544), a National Centre of Competence in Research funded by the Swiss National Science Foundation.

REFERENCES

(1) Morra, E.; Giamello, E.; Chiesa, M. EPR Approaches to Heterogeneous Catalysis. The Chemistry of Titanium in Heterogeneous Catalysts and Photocatalysts. *J. Magn. Reson.* **2017**, *280*, 89–102. https://doi.org/10.1016/j.jmr.2017.02.008.

(2) Manßen, M.; Schafer, L. L. Titanium Catalysis for the Synthesis of Fine Chemicals – Development and Trends. *Chem. Soc. Rev.* **2020**, *49* (19), 6947–6994. https://doi.org/10.1039/D0CS00229A.

(3) McCallum, T.; Wu, X.; Lin, S. Recent Advances in Titanium Radical Redox Catalysis. *J. Org. Chem.* **2019**, *84* (22), 14369–14380. https://doi.org/10.1021/acs.joc.9b02465.

(4) Tonks, I. A. Ti-Catalyzed and -Mediated Oxidative Amination Reactions. *Acc. Chem. Res.* **2021**, *54* (17), 3476–3490. https://doi.org/10.1021/acs.accounts.1c00368.

(5) Clerici, M. G.; Bellussi, G.; Romano, U. Synthesis of Propylene Oxide from Propylene and Hydrogen Peroxide Catalyzed by Titanium Silicalite. *J. Catal.* **1991**, *129* (1), 159–167. https://doi.org/10.1016/0021-9517(91)90019-Z.

(6) Buijink, J. K. F.; Van Vlaanderen, J. J. M.; Crocker, M.; Niele, F. G. M. Propylene Epoxidation over Titanium-on-Silica Catalyst - The Heart of the SMPO Process. *Catal. Today* **2004**, *93–95*, 199–204. https://doi.org/10.1016/j.cattod.2004.06.041.

(7) Böhm, L. L. The Ethylene Polymerization with Ziegler Catalysts: Fifty Years after the Discovery. *Angew. Chemie - Int. Ed.* **2003**, *42* (41), 5010–5030. https://doi.org/10.1002/anie.200300580.

(8) Vogt, C.; Weckhuysen, B. M. The Concept of Active Site in Heterogeneous Catalysis. *Nat. Rev. Chem.* **2022**, *6* (2), 89–111. https://doi.org/10.1038/s41570-021-00340-y.

(9) Wachs, Israel E., and Miguel A. Bañares, eds. *Springer Handbook of Advanced Catalyst Characterization*. Springer Nature, 2023.

(10) Guda, A. A.; Guda, S. A.; Martini, A.; Kravtsova, A. N.; Algasov, A.; Bugaev, A.; Kubrin, S. P.; Guda, L. V.; Šot, P.; van Bokhoven, J. A.; Copéret, C.; Soldatov, A. V. Understanding X-Ray Absorption Spectra by Means of Descriptors and Machine Learning Algorithms. *npj Comput. Mater.* **2021**, *7* (1), 203. https://doi.org/10.1038/s41524-021-00664-9.

(11) Baker, M. L.; Mara, M. W.; Yan, J. J.; Hodgson, K. O.; Hedman, B.; Solomon, E. I. K- and L-Edge X-Ray Absorption Spectroscopy (XAS) and Resonant Inelastic X-Ray Scattering (RIXS) Determination of Differential Orbital Covalency (DOC) of Transition Metal Sites. *Coord. Chem. Rev.* **2017**, *345*, 182–208. https://doi.org/10.1016/j.ccr.2017.02.004.

(12) DeBeer George, S.; Brant, P.; Solomon, E. I. Metal and Ligand K-Edge XAS of Organotitanium Complexes: Metal 4p and 3d Contributions to Pre-Edge Intensity and Their Contributions to Bonding. *J. Am. Chem. Soc.* **2005**, *127* (2), 667–674. https://doi.org/10.1021/ja044827v.

(13) DeBeer George, S.; Huang, K.-W.; Waymouth, R. M.; Solomon, E. I. Metal and Ligand K-Edge XAS of Titanium−TEMPO Complexes: Determination of Oxidation States and Insights into Ti−O Bond Homolysis. *Inorg. Chem.* **2006**, *45* (11), 4468–4477. https://doi.org/10.1021/ic060402t.

(14) Spanjers, C. S.; Guillo, P.; Tilley, T. D.; Janik, M. J.; Rioux, R. M. Identification of Second Shell Coordination in Transition Metal Species Using Theoretical XANES: Example of Ti-O-(C, Si, Ge) Complexes. *J. Phys. Chem. A* **2017**,

121 (1), 162–167. https://doi.org/10.1021/acs.jpca.6b12197.

(15) Farges, F.; Brown, G. E.; Rehr, J. J. Ti K-Edge XANES Studies of Ti Coordination and Disorder in Oxide Compounds: Comparison between Theory and Experiment. *Phys. Rev. B* **1997**, *56* (4), 1809–1819. https://doi.org/10.1103/PhysRevB.56.1809.

(16) Jiang, N.; Su, D.; Spence, J. C. H. Determination of Ti Coordination from Pre-Edge Peaks in Ti K-Edge XANES. *Phys. Rev. B* **2007**, *76* (21), 214117. https://doi.org/10.1103/PhysRevB.76.214117.

(17) Ackerson, M. R.; Cody, G. D.; Mysen, B. O. ^{29}Si Solid State NMR and Ti K-Edge XAFS Pre-Edge Spectroscopy Reveal Complex Behavior of Ti in Silicate Melts. *Prog. Earth Planet. Sci.* **2020**, *7,* 14. https://doi.org/10.1186/s40645-020-00326-2.

(18) Gromilov, S. A.; Baidina, I. A. Regularities of Crystal Structures of Cu(II) β-Diketonates. *J. Struct. Chem.* **2004**, *45* (6), 1031–1081. https://doi.org/10.1007/s10947-005-0096-4.

(19) Noh, H. J.; Kang, J. S.; Lee, S. S.; Kim, G.; Han, S. W.; Oh, S. J.; Kim, J. Y.; Lee, H. G.; Yeo, S.; Guha, S.; Cheong, S. W. Valence Values of the Cations in Selenospinel Cu(Cr,Ti)2Se 4. *Epl* **2007**, *78* (2), 0–6. https://doi.org/10.1209/0295-5075/78/27004.

(20) Raval, P. Y.; Joshi, N. P.; Pansara, P. R.; Vasoya, N. H.; Kumar, S.; Dolia, S. N.; Modi, K. B.; Singhal, R. K. A Ti L3,2 - and K- Edge XANES and EXAFS Study on Fe3+ - Substituted CaCu3Ti4O12. *Ceram. Int.* **2018**, *44* (17), 20716–20722. https://doi.org/10.1016/j.ceramint.2018.08.066.

(21) Henderson, G. S.; Liu, X.; Fleet, M. E. A Ti L-Edge X-Ray Absorption Study of Ti-Silicate Glasses. *Phys. Chem. Miner.* **2002**, *29* (1), 32–42. https://doi.org/10.1007/s002690100208.

(22) Mo, L.-B.; Bai, Y.; Xiang, Q.-Y.; Li, Q.; Wang, J.-O.; Ibrahim, K.; Cao, J.-L. Band Gap Engineering of TiO 2 through Hydrogenation. *Appl. Phys. Lett.* **2014**, *105* (20), 202114. https://doi.org/10.1063/1.4902445.

(23) Van Spronsen, M. A.; Zhao, X.; Jaugstetter, M.; Escudero, C.; Duchoň, T.; Hunt, A.; Waluyo, I.; Yang, P.; Tschulik, K.; Salmeron, M. B. Interface Sensitivity in Electron/Ion Yield X-Ray Absorption Spectroscopy: The TiO2-H2O Interface. *J. Phys. Chem. Lett.* **2021**, *12* (41), 10212–10217. https://doi.org/10.1021/acs.jpclett.1c02115.

(24) Ikeno, H.; De Groot, F. M. F.; Tanaka, I. Ab-Initio CI Calculations for 3d Transition Metal $L_{2,3}$ X-Ray Absorption Spectra of $TiCl_4$ and $VOCl_3$. *J. Phys. Conf. Ser.* **2009**, *190*. No. 012005 https://doi.org/10.1088/1742-6596/190/1/012005.

(25) Casarin, M.; Finetti, P.; Vittadini, A.; Wang, F.; Ziegler, T. Spin−Orbit Relativistic Time-Dependent Density Functional Calculations of the Metal and Ligand Pre-Edge XAS Intensities of Organotitanium Complexes: TiCl 4 , Ti(η 5 -C 5 H 5)Cl 3 , and Ti(η 5 -C 5 H 5) 2 Cl 2. *J. Phys. Chem. A* **2007**, *111* (24), 5270–5279. https://doi.org/10.1021/jp071561g.

(26) Xu, Z.; Romankov, V.; Doll, A.; Dreiser, J. Orienting Dilute Thin Films of Non-Planar Spin-1/2 Vanadyl–Phthalocyanine Complexes. *Mater. Adv.* **2022**, *3* (12), 4938–4946. https://doi.org/10.1039/D2MA00157H.

(27) Pickup, D. F.; Zegkinoglou, I.; Ballesteros, B.; Ganivet, C. R.; García-Lastra, J. M.; Cook, P. L.; Johnson, P. S.; Rogero, C.; de Groot, F.; Rubio, A.; de la Torre, G.; Ortega, J. E.; Himpsel, F. J. Influence of Axial and Peripheral Ligands on the Electronic Structure of Titanium Phthalocyanines. *J. Phys. Chem. C* **2013**, *117* (9), 4410–4420. https://doi.org/10.1021/jp3117853.

(28) Piovano, A.; Signorile, M.; Braglia, L.; Torelli, P.; Martini, A.; Wada, T.; Takasao, G.; Taniike, T.; Groppo, E. Electronic Properties of Ti Sites in Ziegler–Natta Catalysts. *ACS Catal.* **2021**, *11* (15), 9949–9961. https://doi.org/10.1021/acscatal.1c01735.

(29) Bittencourt, C.; Krüger, P.; Lagos, M. J.; Ke, X.; Van Tendeloo, G.; Ewels, C.; Umek, P.; Guttmann, P. Towards Atomic Resolution in Sodium Titanate Nanotubes Using Near-Edge X-Ray-Absorption Fine-Structure Spectromicroscopy Combined with Multichannel Multiple-Scattering Calculations. *Beilstein J. Nanotechnol.* **2012**, *3* (1), 789–797. https://doi.org/10.3762/bjnano.3.88.

(30) Ji, H.; Ni, J.; Zhao, D.; Liu, W. Application of Titanate Nanotubes for Photocatalytic Decontamination in Water: Challenges and Prospects. *ACS ES&T Eng.* **2022**, *2* (6), 1015–1038. https://doi.org/10.1021/acsestengg.1c00451.

(31) Signorile, M.; Braglia, L.; Crocellà, V.; Torelli, P.; Groppo, E.; Ricchiardi, G.; Bordiga, S.; Bonino, F. Titanium Defective Sites in TS-1: Structural Insights by Combining Spectroscopy and Simulation. *Angew. Chemie Int. Ed.* **2020**, *59* (41), 18145–18150. https://doi.org/10.1002/anie.202005841.

(32) Lätsch, L.; Kaul, C. J.; Yakimov, A. V.; Müller, I. B.; Hassan, A.; Perrone, B.; Aghazada, S.; Berkson, Z. J.; De Baerdemaeker, T.; Parvulescu, A.-N.; Seidel, K.; Teles, J. H.; Copéret, C. NMR Signatures and Electronic Structure of Ti Sites in Titanosilicalite-1 from Solid-State 47/49 Ti NMR Spectroscopy. *J. Am. Chem. Soc.* **2023**, *145* (28), 15018–15023. https://doi.org/10.1021/jacs.2c09867.

(33) Noh, G.; Lam, E.; Alfke, J. L.; Larmier, K.; Searles, K.; Wolf, P.; Copéret, C. Selective Hydrogenation of CO 2 to CH 3 OH on Supported Cu Nanoparticles Promoted by Isolated Ti IV Surface Sites on SiO 2. *ChemSusChem* **2019**, *12* (5), 968–972. https://doi.org/10.1002/cssc.201900134.

(34) Pathak, M.; Bohra, R.; Mehrotra, R. C.; Lorenz, I.-P.; Piotrowski, H. Synthetic Studies and Structural Aspects of Novel Metallacyclic Compoundsof Titanium(IV) Incorporating Nitrogen, Oxygen and Sulphur: 1. Reactions of Cis-Dialkoxy-Bis(Acetylacetonato)Titanium(IV) with Alkoxyalkanols and the Crystal Structure of a New Modif. *Transit. Met. Chem.* **2003**, No. 28, 187–192.

(35) Stauber, J. M.; Cummins, C. C. Terminal Titanyl Complexes of Tri- and Tetrametaphosphate: Synthesis, Structures, and Reactivity with Hydrogen Peroxide. *Inorg. Chem.* **2017**, *56* (5), 3022–3029. https://doi.org/10.1021/acs.inorgchem.6b03149.

(36) Lansing, M.; Engler, H.; Leuther, T. M.; Neudörfl, J.-M.; Berkessel, A. Titanium Cis -1,2-Diaminocyclohexane Salalen Catalysts of Outstanding Activity and Enantioselectivity for the Asymmetric Epoxidation of Nonconjugated Terminal Olefins with Hydrogen Peroxide. *ChemCatChem* **2016**, *8* (24), 3706–3709. https://doi.org/10.1002/cctc.201601154.

(37) Engler, H.; Lansing, M.; Gordon, C. P.; Neudörfl, J.-M.; Schäfer, M.; Schlörer, N. E.; Copéret, C.; Berkessel, A. Olefin Epoxidation Catalyzed by Titanium–Salalen Complexes: Synergistic H 2 O 2 Activation by Dinuclear Ti Sites, Ligand H-Bonding, and π-Acidity. *ACS Catal.* **2021**, *11* (6), 3206–3217. https://doi.org/10.1021/acscatal.0c05320.

(38) Talsi, E. P.; Bryliakova, A. A.; Bryliakov, K. P. Titanium Salan/Salalen Complexes: The Twofaced Janus of Asymmetric Oxidation Catalysis. *Chem. Rec.* **2016**, *16* (2), 924–939. https://doi.org/10.1002/tcr.201500273.

(39) Glidewell, C.; Turner, G. M.; Ferguson, G. Racemic Cis-Dichlorobis(2,2,6,6-Tetramethyl-3,5-Heptanedionato)Titanium(IV). *Acta Crystallogr. Sect. C Cryst. Struct. Commun.* **1996**, *52* (1), 11–14. https://doi.org/10.1107/S0108270195012224.

(40) Davlieva, M. G.; Lindeman, S. V.; Neretin, I. S.; Kochi, J. K. Isolation, X-Ray Structures, and Electronic Spectra of Reactive Intermediates in Friedel−Crafts Acylations. *J. Org. Chem.* **2005**, *70* (10), 4013–4021. https://doi.org/10.1021/jo0501588.

(41) McLeod, J. A.; Moewes, A.; Zatsepin, D. A.; Kurmaev, E. Z.; Wypych, A.; Bobowska, I.; Opasinska, A.; Cholakh, S. O. Predicting the Band Gap of Ternary Oxides Containing 3d10 and 3d0 Metals. *Phys. Rev. B* **2012**, *86* (19), 195207. https://doi.org/10.1103/PhysRevB.86.195207.

(42) de Groot, F. M. F.; Fuggle, J. C.; Thole, B. T.; Sawatzky, G. A. L2,3 x-Ray-Absorption Edges of D0 Compounds: K+, Ca2+, Sc3+, and Ti4+ in Oh (Octahedral) Symmetry. *Phys. Rev. B* **1990**, *41* (2), 928–937. https://doi.org/10.1103/PhysRevB.41.928.

(43) Laskowski, R.; Blaha, P. Understanding the L2,3 x-Ray Absorption Spectra of Early 3d Transition Elements. *Phys. Rev. B - Condens. Matter Mater. Phys.* **2010**, *82* (20), 1–6. https://doi.org/10.1103/PhysRevB.82.205104.

(44) Krüger, P. Multichannel Multiple Scattering Calculation of L2,3 -Edge Spectra of TiO2 and SrTiO3: Importance of Multiplet Coupling and Band Structure. *Phys. Rev. B - Condens. Matter Mater. Phys.* **2010**, *81* (12), 1–6. https://doi.org/10.1103/PhysRevB.81.125121.

(45) Kroll, T.; Solomon, E. I.; De Groot, F. M. F. Final-State Projection Method in Charge-Transfer Multiplet Calculations: An Analysis of Ti L-Edge Absorption Spectra. *J. Phys. Chem. B* **2015**, *119* (43), 13852–13858. https://doi.org/10.1021/acs.jpcb.5b04133.

(46) de Groot, F. M. F.; Elnaggar, H.; Frati, F.; Wang, R. pan; Delgado-Jaime, M. U.; van Veenendaal, M.; Fernandez-Rodriguez, J.; Haverkort, M. W.; Green, R. J.; van der Laan, G.; Kvashnin, Y.; Hariki, A.; Ikeno, H.; Ramanantoanina, H.; Daul, C.; Delley, B.; Odelius, M.; Lundberg, M.; Kuhn, O.; Bokarev, S. I.; Shirley, E.; Vinson, J.; Gilmore, K.; Stener, M.; Fronzoni, G.; Decleva, P.; Kruger, P.; Retegan, M.; Joly, Y.; Vorwerk, C.; Draxl, C.; Rehr, J.; Tanaka, A. 2P X-Ray Absorption Spectroscopy of 3D Transition Metal Systems. *J. Electron Spectros. Relat. Phenomena* **2021**, *249* (March), 147061. https://doi.org/10.1016/j.elspec.2021.147061.

(47) Wasinger, E. C.; de Groot, F. M. F.; Hedman, B.; Hodgson, K. O.; Solomon, E. I. L-Edge X-Ray Absorption Spectroscopy of Non-Heme Iron Sites: Experimental Determination of Differential Orbital Covalency. *J. Am. Chem. Soc.* **2003**, *125* (42), 12894–12906. https://doi.org/10.1021/ja034634s.

(48) Lundberg, M.; Kroll, T.; DeBeer, S.; Bergmann, U.; Wilson, S. A.; Glatzel, P.; Nordlund, D.; Hedman, B.; Hodgson, K. O.; Solomon, E. I. Metal–Ligand Covalency of Iron Complexes from High-Resolution Resonant Inelastic X-Ray Scattering. *J. Am. Chem. Soc.* **2013**, *135* (45), 17121–17134. https://doi.org/10.1021/ja408072q.

(49) Kroll, T.; Baker, M. L.; Wilson, S. A.; Lundberg, M.; Juhin, A.; Arrio, M.-A.; Yan, J. J.; Gee, L. B.; Braun, A.; Weng, T.-C.; Sokaras, D.; Hedman, B.; Hodgson, K. O.; Solomon, E. I. Effect of 3d/4p Mixing on 1s2p Resonant Inelastic X-Ray Scattering: Electronic Structure of Oxo-Bridged Iron Dimers. *J. Am. Chem. Soc.* **2021**, *143* (12), 4569–4584. https://doi.org/10.1021/jacs.0c11193.

(50) Smeltz, J. L.; Lilly, C. P.; Boyle, P. D.; Ison, E. A. The Electronic Nature of Terminal Oxo Ligands in Transition-Metal Complexes: Ambiphilic Reactivity of Oxorhenium Species. *J. Am. Chem. Soc.* **2013**, *135* (25), 9433–9441. https://doi.org/10.1021/ja401390v.

(51) Tanaka, A.; Jo, T. Resonant 3 d , 3 p and 3 s Photoemission in Transition Metal Oxides Predicted at 2 p Threshold. *J. Phys. Soc. Japan* **1994**, *63* (7), 2788–2807. https://doi.org/10.1143/JPSJ.63.2788.

(52) Cowan, R. D. Theoretical Calculation of Atomic Spectra Using Digital Computers*. *J. Opt. Soc. Am.* **1968**, *58* (6), 808. https://doi.org/10.1364/josa.58.000808.

(53) Haverkort, M. W.; Zwierzycki, M.; Andersen, O. K. Multiplet Ligand-Field Theory Using Wannier Orbitals. *Phys. Rev. B - Condens. Matter Mater. Phys.* **2012**, *85* (16), 1–20. https://doi.org/10.1103/PhysRevB.85.165113.

(54) Fernández-Rodríguez, J.; Toby, B.; Van Veenendaal, M. Xclaim: A Graphical Interface for the Calculation of Core-Hole Spectroscopies. *J. Electron Spectros. Relat. Phenomena* **2015**, *202*, 81–88. https://doi.org/10.1016/j.elspec.2015.03.010.

(55) Stavitski, E.; de Groot, F. M. F. The CTM4XAS Program for EELS and XAS Spectral Shape Analysis of Transition Metal L Edges. *Micron* **2010**, *41* (7), 687–694. https://doi.org/10.1016/j.micron.2010.06.005.

(56) Roemelt, M.; Maganas, D.; Debeer, S.; Neese, F. A Combined DFT and Restricted Open-Shell Configuration Interaction Method Including Spin-Orbit Coupling: Application to Transition Metal L-Edge X-Ray Absorption Spectroscopy. *J. Chem. Phys.* **2013**, *138*, 204101. https://doi.org/10.1063/1.4804607.

(57) Ramanantoanina, H.; Daul, C. A Non-Empirical Calculation of 2p Core-Electron Excitation in Compounds with 3d Transition Metal Ions Using Ligand-Field and Density Functional Theory (LFDFT). *Phys. Chem. Chem. Phys.* **2017**, *19* (31), 20919–20929. https://doi.org/10.1039/c7cp03140h.

(58) Gilmore, K.; Vinson, J.; Shirley, E. L.; Prendergast, D.; Pemmaraju, C. D.; Kas, J. J.; Vila, F. D.; Rehr, J. J. Efficient Implementation of Core-Excitation Bethe-Salpeter Equation Calculations. *Comput. Phys. Commun.* **2015**, *197*, 109–117. https://doi.org/10.1016/j.cpc.2015.08.014.

(59) Hariki, A.; Winder, M.; Kuneš, J. Continuum Charge Excitations in High-Valence Transition-Metal Oxides Revealed by Resonant Inelastic X-Ray Scattering. *Phys. Rev. Lett.* **2018**, *121* (12), 3–8. https://doi.org/10.1103/PhysRevLett.121.126403.

(60) Guo, M.; Källman, E.; Pinjari, R. V.; Couto, R. C.; Kragh Sørensen, L.; Lindh, R.; Pierloot, K.; Lundberg, M. Fingerprinting Electronic Structure of Heme Iron by Ab Initio Modeling of Metal L-Edge X-Ray Absorption Spectra. *J. Chem. Theory Comput.* **2019**, *15* (1), 477–489. https://doi.org/10.1021/acs.jctc.8b00658.

(61) Perdew, J. P.; Burke, K.; Ernzerhof, M. Generalized Gradient Approximation Made Simple. *Phys. Rev. Lett.* **1996**, *77* (18), 3865–3868. https://doi.org/10.1103/PhysRevLett.77.3865.

(62) Marzari, N.; Mostofi, A. A.; Yates, J. R.; Souza, I.; Vanderbilt, D. Maximally Localized Wannier Functions: Theory and Applications. *Rev. Mod. Phys.* **2012**, *84* (4), 1419–1475. https://doi.org/10.1103/RevModPhys.84.1419.

(63) Gordon, C. P.; Engler, H.; Tragl, A. S.; Plodinec, M.; Lunkenbein, T.; Berkessel, A.; Teles, J. H.; Parvulescu, A. N.; Copéret, C. Efficient Epoxidation over Dinuclear Sites in Titanium Silicalite-1. *Nature* **2020**, *586* (7831), 708–713. https://doi.org/10.1038/s41586-020-2826-3.

(64) Sofetis, A.; Fotopoulou, F.; Raptopoulou, C. P.; Zafiropoulos, T. F.; Perlepes, S. P.; Klouras, N. Reactions of Titanocene Dihalides with N,N′,N″-Chelates: Preparation, X-Ray Structure and Characterization of Bis(Chloro){2,6-Bis[(3,5-Dimethyl)Pyrazol-1-Yl]Pyridine}(H2-Peroxo)Titanium(IV). *Polyhedron* **2009**, *28* (15), 3356–3360. https://doi.org/10.1016/j.poly.2009.05.048.

.